Check for updates

ADVANCED FUNCTIONAL MATERIALS
www.afm-journal.de

Active Learning-Driven Discovery of Sub-2 Nm High-Entropy Nanocatalysts for Alkaline Water Splitting

Sakthivel Perumal, Da Bean Han, Thandapani Marimuthu, Taewaen Lim, Hyun Woo Kim, and Junhyeok Seo**

High-entropy nanoparticles (HENPs) present a vast opportunity for the development of advanced electrocatalysts. The optimization of their chemical compositions, including the careful selection and combination of elements, is critical to tailoring HENPs for specific catalytic processes. To reduce the extensive experimental effort involved in composition optimization, active learning techniques can be utilized to predict and suggest materials with enhanced electrocatalytic activity. In this study, sub-2 nm high-entropy catalysts incorporating eight transition metal elements are developed through an active learning workflow aimed at identifying optimal compositions. Using initial experimental data, the approach successfully guided the discovery of a new octonary HENP catalyst with state-of-the-art performance in the hydrogen evolution reaction (HER). Catalyst performance is improved within the prediction uncertainty of the machine learning model. For the oxygen evolution reaction (OER), however, the initial model demonstrated limited predictive accuracy, leading to an assessment of the workflow's boundaries. These findings underscore how the integration of curated experimental data with active learning can accelerate electrocatalyst discovery, while also highlighting critical areas for further model refinement.

1. Introduction

High-entropy materials (HEMs) are an emerging class of electrocatalysts that offer expansive compositional flexibility, allowing for precise tuning of catalytic properties.[1] Characterized by unique attributes such as high entropy, lattice distortion, sluggish diffusion, and the "cocktail effect", HEMs exhibit impressive catalytic performance.[2–4] With five or more multi-element active sites dispersed across complex surfaces, HEMs provide a quasi-continuum of adsorption energies for reaction intermediates.[5] By modulating their elemental compositions, researchers can tailor electronic structures and adsorption energies to design highly efficient catalysts.[6] This adaptability is particularly advantageous for electrocatalytic water splitting, a promising route for renewable hydrogen gas (H_2) production that is essential for establishing carbon-neutral energy systems.[7] However, identifying optimal compositions within the vast range of element combinations possible in HEMs presents a substantial challenge, making experimental exploration practically infeasible within realistic timeframes.[8] To address this complexity, artificial intelligence (AI) and machine learning (ML) models can be utilized to predict catalytic activity based on limited yet expanding datasets. Recent advances in AI and ML have been made to discover heterogeneous catalysts using AI and high throughput screening (HTS), which can be found in recent research and review articles.[9–16] However, accurate modeling of the catalytic activity of such diverse and complex surfaces still requires further development.

Recent efforts to pinpoint optimal HEM compositions have incorporated density functional theory (DFT) with ML models.[17–19] However, this approach has limitations, especially with amorphous materials where critical catalytic descriptors such as overpotential and turnover frequency are experimentally measurable yet challenging to calculate through DFT. The vast compositional space and stoichiometric variability in HEMs further limit DFT's applicability. While data from published studies are valuable, generating high-quality, comprehensive datasets for new HEMs remains a significant hurdle. Additionally, inconsistencies in catalyst data are common,[20,21] as similar compositions can exhibit variable performance due to

S. Perumal, D. B. Han, T. Marimuthu, T. Lim, H. W. Kim, J. Seo
Department of Chemistry
Gwangju Institute of Science and Technology
Gwangju 61005, Republic of Korea
E-mail: hwk@gist.ac.kr; seojh@gist.ac.kr

H. W. Kim
Center for Quantum Technology
Korea Institute of Science and Technology (KIST)
Seoul 02792, South Korea

J. Seo
Research Center for Innovative Energy and Carbon Optimized Synthesis for Chemicals
(Inn-ECOSysChem)
Gwangju Institute of Science and Technology
Gwangju 61005, Republic of Korea

The ORCID identification number(s) for the author(s) of this article can be found under https://doi.org/10.1002/adfm.202424887

© 2025 The Author(s). Advanced Functional Materials published by Wiley-VCH GmbH. This is an open access article under the terms of the Creative Commons Attribution-NonCommercial-NoDerivs License, which permits use and distribution in any medium, provided the original work is properly cited, the use is non-commercial and no modifications or adaptations are made.

DOI: 10.1002/adfm.202424887

differences in experimental conditions, including electrode materials, electrolytes, and applied potentials.[22] To overcome these challenges, we developed ML models based on experimental datasets, aiming to enhance predictive accuracy and mitigate inconsistency in the discovery of novel, efficient catalysts. Nonetheless, generating extensive experimental datasets is both time-intensive and costly. In such cases, an active learning framework that integrates ML with parallel experimental workflows is a promising solution. This closed-loop approach combines limited data, AI, and human expertise.[23–26] Through active learning, the model iteratively samples the design space to refine predictions, even when initial model coverage is limited. Employing Bayesian optimization (BO), this approach trains a surrogate ML model on a small dataset, using acquisition functions to select untested, representative compositions. Consequently, the model improves its accuracy and generalizability across unexplored compositions,[27,28] striking a balance between exploration and exploitation within vast search spaces, ultimately accelerating catalyst discovery.[29] Recent applications of BO toward the discovery of alloy catalysts have been made. For instance, BO was applied to explore alloy catalysts for water splitting.[30] In addition, the BO was utilized to discover catalytic HEMs with multiple objectives[31] and DFT calculations.[10] As shown in successful examples, BO offers significant advantages when used with relatively small data sets while ML methods such as reinforcement learning require large data sets.[32] In addition, genetic algorithms (GA) can be used with computationally efficient methods to solve the optimization problem in materials discovery.[33]

Ultra-small nanoparticles are gaining attention in electrocatalysis for their distinct advantages.[34–36] As nanoparticle size decreases, surface area and atomic utilization efficiency increase, exposing a large number of active sites and enhancing catalytic performance.[37] We hypothesize that synthesizing ultra-small high-entropy nanoparticles (HENPs) could further amplify catalytic activity by combining the benefits of reduced particle size with HEMs' unique properties. However, these nanoparticles face significant synthetic challenges, including aggregation and thermodynamic instability at elevated temperatures.[38] To address these challenges, we adopted a polyol synthesis method, which is simple, cost-effective, low-temperature process, and time-efficient.[39]

Our novel octonary HENP catalysts were designed using five non-noble metals (Al, Sn, Co, Ni, Cu, Ce) and two noble metals (Ir, Rh) based on the concept of high-entropy alloys to explore optimal compositions for water electrolysis, minimizing noble metal use. The HENP catalysts leverage the synergistic effects of multiple metals to enhance catalytic performance, and the combination of noble and non-noble metals balances performance and affordability.[40]

This study leverages a Bayesian optimization-based ML model, combined with systematic experimental data, to develop a predictive model for optimized HENP precursor compositions and catalytic performance in water electrolysis. Seventy datasets were generated through high-throughput experiments under consistent synthetic and testing conditions to train and validate the ML model, which subsequently predicted the overpotential for a new octonary system. After 200 iterations, optimal precursor compositions were identified and experimentally validated. The final precursor composition for the hydrogen evolution reaction (HER) catalyst exhibited an overpotential of 12 mV, while the oxygen evolution reaction (OER) catalyst demonstrated an overpotential of 239 mV at a current density of 10 mA cm^{-2}. These results reveal superior catalytic performance compared to commercial Pt/C and IrO_2 catalysts, respectively.

2. Results and Discussion

2.1. Optimal Composition of HENPs via Bayesian Optimization

Bayesian optimization (BO) algorithm combined with experimental testing was applied to identify the optimal precursor composition of HENP electrocatalysts for minimizing HER and OER overpotentials in alkaline water splitting. The conceptual design of this study is illustrated in **Figure 1**, encompassing i) catalyst synthesis and performance analysis, ii) integration of BO method, and iii) validation and characterization. Figure 1a outlines the workflow for discovering low-overpotential HENPs for alkaline water splitting. Eight distinct metal chloride precursors were selected, with their molar concentrations varied randomly during the synthesis (Figure 1b). The HENPs were synthesized via a polyol method, with $NaBH_4$ serving as a reducing agent. This process facilitated the reduction of metal ions to isolated atoms, which then coalesced to form nuclei. After a 2-h reaction at 230 °C, the HENPs were generated as black precipitates. Electrochemical analysis was conducted to measure HER and OER overpotentials at 10 mA cm^{-2} via linear sweep voltammetry (LSV) in a 1M KOH electrolyte (Figure 1c). LSV curves for minimum (HENPs: y) and maximum (HENPs: x) overpotentials are shown in Figure 1c, while complete datasets, including LSV curves and overpotential values with corresponding precursor compositions, are provided in the Supporting Information (Figures S1 and S2; Table S1, Supporting Information). The BO process, illustrated in Figure 1d, utilized the molar concentrations of precursors and their experimentally measured overpotential values as input data. Gaussian Process Regression (GPR) was employed to predict relationships between the 8-D precursor composition vectors and overpotential values.

This GPR model enabled control over process parameters,[41] while the upper confidence bound (UCB) acquisition function proposed compositions for subsequent testing by balancing predicted outcomes from the surrogate model with associated uncertainties.[42] Through iterative updates, the acquisition function identified the next composition of interest, and 200 optimization iterations were sufficient to discover locally optimal compositions.[43] Three input datasets were utilized in this study: two targeting the HER and one targeting the OER (Tables S1–S3, Supporting Information). Based on the experimental precursor composition and performance data, we identified 10 optimal precursor compositions in each case using BO process (Tables S2–S4; Figures S3 and S4, Supporting Information). We began by evaluating the GPR model's performance and analyzing the influence of individual metal elements (input variables) on HER overpotential, as shown in **Figure 2**. The HER overpotential predictions for the suggested catalysts were assessed, and the contribution of the eight con-

© 2025 The Author(s). Advanced Functional Materials published by Wiley-VCH GmbH

16163028, 0, Downloaded from https://advanced.onlinelibrary.wiley.com/doi/10.1002/adfm.202424887 by Junhyeok Seo - Gwangju Institute Of Science And Technology (Gist) , Wiley Online Library on [18/03/2025]. See the Terms and Conditions (https://onlinelibrary.wiley.com/terms-and-conditions) on Wiley Online Library for rules of use; OA articles are governed by the applicable Creative Commons License

16163028, 0, Downloaded from https://advanced.onlinelibrary.wiley.com/doi/10.1002/adfm.202424887 by Junhyeok Seo - Gwangju Institute Of Science And Technology (Gist) , Wiley Online Library on [18/03/2025]. See the Terms and Conditions (https://onlinelibrary.wiley.com/terms-and-conditions) on Wiley Online Library for rules of use; OA articles are governed by the applicable Creative Commons License

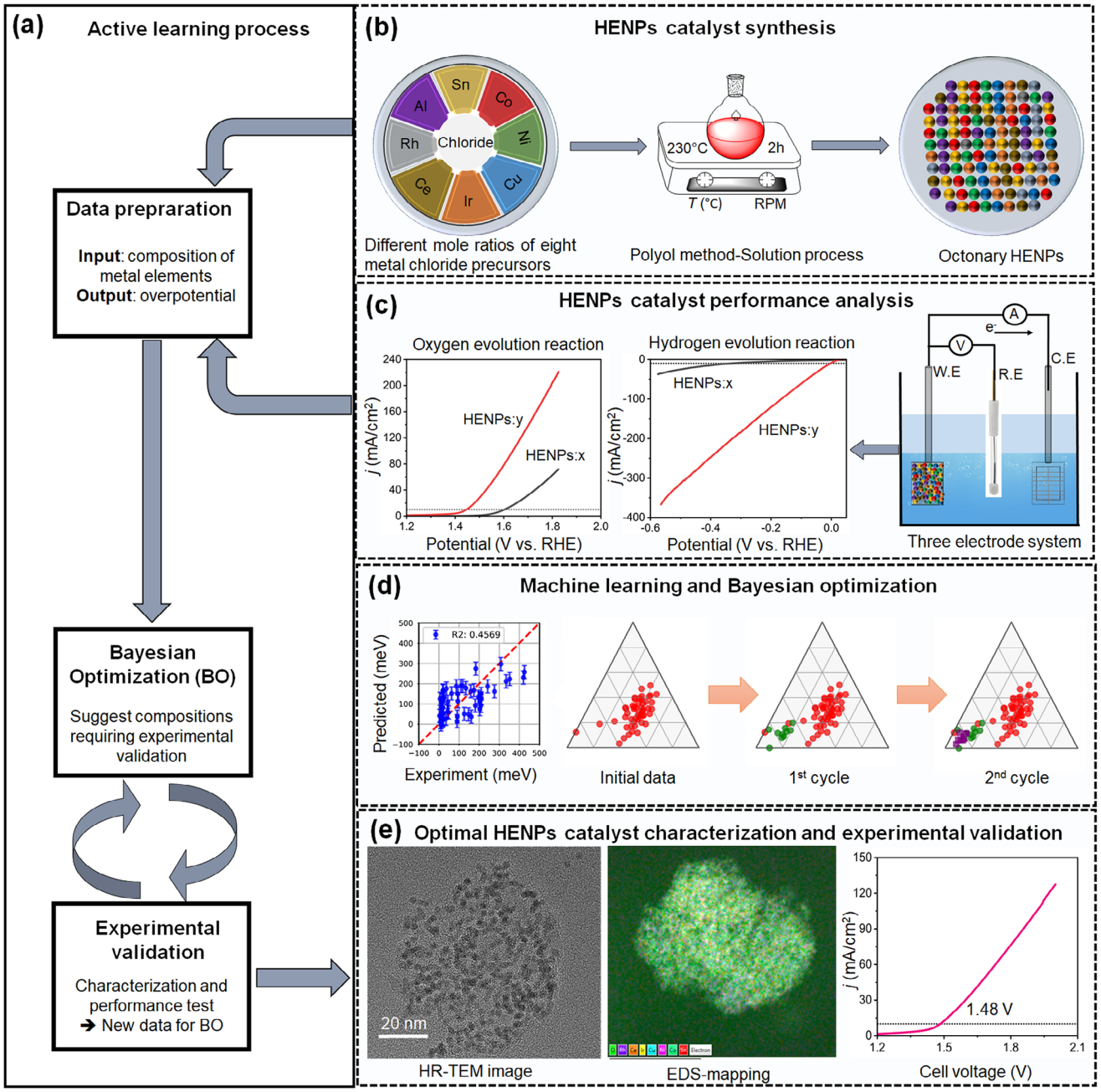

Figure 1. Conceptual design of this work, a) workflow for searching low overpotential HENPs catalysts for alkaline water splitting, b) schematic of the HENPs nanoparticle synthesis, c) HER and OER performance analysis, linear sweep voltammetry curves of HENPs with minimum (HENPs: y) and maximum (HENPs: x) overpotential, d) active learning through BO and e) HR-TEM images of ultra-small HENPs, EDS mapping, and LSV curves of overall alkaline water splitting.

stituent metal elements was analyzed using SHapely Additive exPlanations (SHAP).[44] Before we begin, two regression models, GPR and XGBoost (a widely used decision tree-based algorithm), were compared as surrogate model in BO. The GPR model outperformed XGBoost for this dataset and was therefore adopted as the regression model throughout this work (Figure 2a,b; Figure S5, Supporting Information). While the GPR model effectively predicted HER overpotentials, it struggled to predict OER overpotentials (Figure 2a,b; Figure S6, Supporting Information), likely due to limitations in the training dataset or feature vectors. Increasing the number of tested metal compositions could improve prediction accuracy; however, generating such data is a labor-intensive process that exceeds the scope of this work, which aims to optimize electrocatalysts using a small, laboratory-scale dataset. Additionally, this suggests that OER overpotential is influenced by factors beyond metal composition alone, in contrast to HER. Thus, a more comprehensive feature vector was prepared

 © 2025 The Author(s). Advanced Functional Materials published by Wiley-VCH GmbH

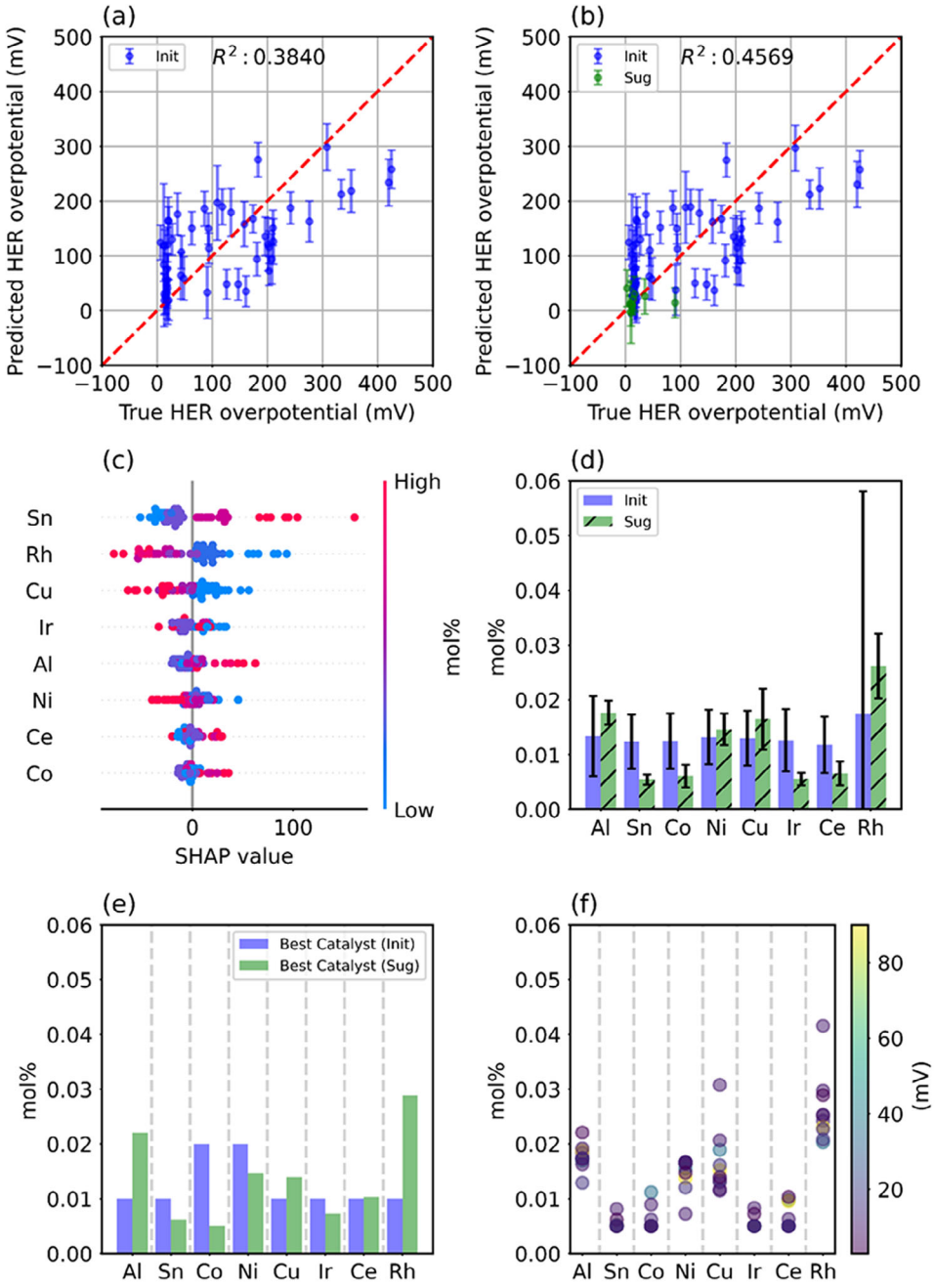

Figure 2. Prediction using the GPR model and Leave-One-Out Cross-Validation (LOOCV) with a) 50 initial and b) 10 suggested catalysts proposed by optimization (a total of 60 catalysts). c) SHAP analysis to determine the effect of each metal element on the HER overpotential. The concentration of the element is shown as a color bar on the right side. d) Average mol% of elements in initial (blue) and suggested catalysts (green), e) mol% of elements in catalyst with lowest HER overpotential in initial (blue) and suggested catalysts (green), and f) the mol% of element in 10 suggested catalysts. All HER overpotential values are validated through experiments.

using the physical properties of the elements. The feature vector with metal composition and physical properties improved the prediction performance of OER. However, the performance of the GPR model was not satisfactory to be used for BO of catalysts for OER (Figure S7, Supporting Information). This implies that the generation of more experimental data may be required, which is beyond the scope of this work. This aspect could be addressed in future research. Consequently, BO was applied to optimize HENP performance for HER, leaving OER optimization for future studies. Including the BO-suggested catalysts in the training dataset enhanced the predictive accuracy of the GPR model (Figure 2b). With the model reasonably predicting HER performance, we quantitatively analyzed the impact of individual metal components on

© 2025 The Author(s). Advanced Functional Materials published by Wiley-VCH GmbH

16163028, 0, Downloaded from https://advanced.onlinelibrary.wiley.com/doi/10.1002/adfm.202424887 by Junhyeok Seo - Gwangju Institute Of Science And Technology (Gist) , Wiley Online Library on [18/03/2025]. See the Terms and Conditions (https://onlinelibrary.wiley.com/terms-and-conditions) on Wiley Online Library for rules of use; OA articles are governed by the applicable Creative Commons License

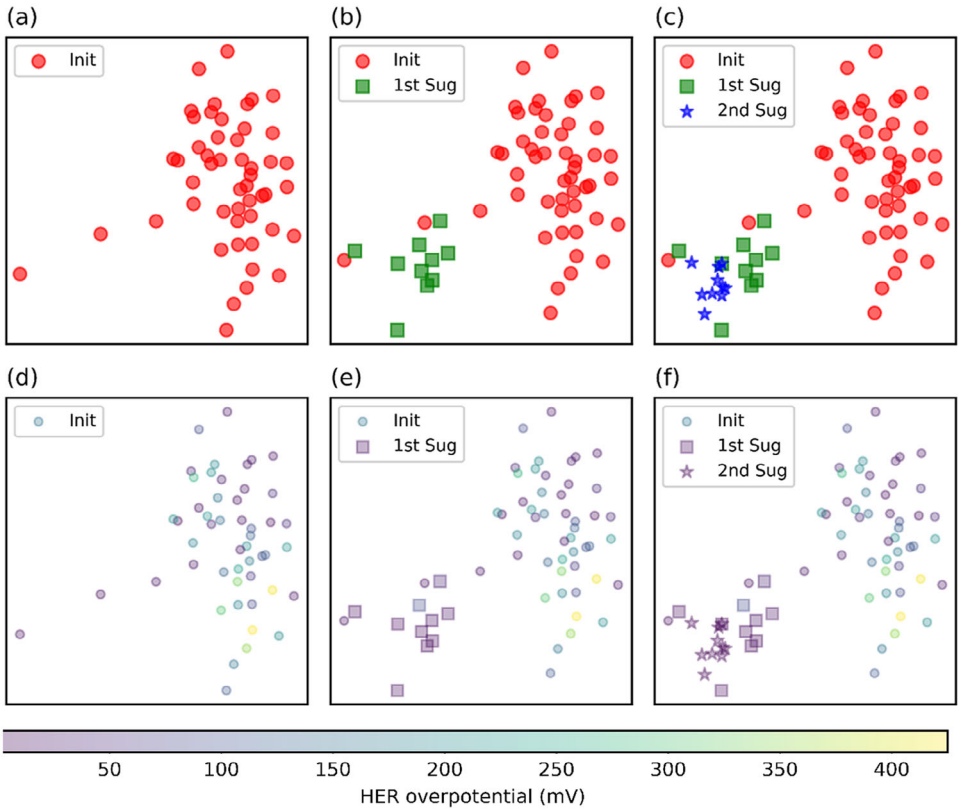

Figure 3. Distribution of catalysts in a) training dataset (denoted as Init), b) newly suggested data from the first round (denoted as 1st Sug) added to (a), and (c) newly suggested data from the second rounds (denoted as 2nd Sug) added to (b). d–f) For the catalyst distributions illustrated in (a–c), the different coloring scheme was adopted based on the overpotential (mV) values.

overpotential using the SHAP values (Figure 2c). SHAP value was used as a measure of the effect of each input variable on the target outcome.[45]

For a given metal element, a positive SHAP value indicates a proportional relationship between its content and HER overpotential, while a negative value indicates an inverse relationship. Larger absolute SHAP value denotes a greater influence on the target variable. This analysis revealed that lower Sn content and higher Rh and Cu content generally improved the HER performance, highlighting opportunities for further catalyst development. By incorporating insights from SHAP analysis and BO, our study demonstrates a robust approach for optimizing HENPs with minimal experimental effort. Total 60 catalysts were used in SHAP analysis, and 10 suggested catalysts proposed by BO were evaluated experimentally to calculate their HER overpotential. On average, the proposed catalysts contained lower Sn content and higher Al, Cu and Rh content. This trend was evident when comparing the elemental composition of the initial catalysts with those suggested by BO (Figure 2d). Additionally, a comparison between the best-performing catalysts before and after BO revealed notable differences in Al and Rh content (Figure 2e). According to the SHAP analysis, an increased Al content increases the HER overpotential, whereas Rh had an inverse effect (Figure 2c). These observations indicate that the results achieved an effective balance between exploitation and exploration within the BO framework in the chemical space. The distribution of the 10 catalysts proposed in the initial BO iteration highlighted the convergence in the content of Sn, Co, Ir, and Ce, while the composition of other elements displayed variability (Figure 2f).

To visualize the training data and newly proposed compositions, dimensionality reduction was performed using the t-distributed Stochastic Neighbor Embedding (t-SNE) method.[46] This method was adopted because of the inherent difficulties in visualizing and analyzing the 8-D vectors in the search space, which corresponds to the number of metal elements. The initial dataset (represented by circles) and the compositions suggested through BO (represented by squares and stars) were shown in **Figure 3**, alongside catalyst performance. The t-SNE analysis revealed clustering patterns among the catalysts, with the BO-suggested catalysts forming clusters near those exhibiting superior performance. This observation suggests that BO effectively proposed new compositions based on the provided dataset. The compositions identified through BO were subsequently validated experimentally, and their surface properties were characterized as described later. The t-SNE results provided insight into the patterns present within the catalyst compositions. Interestingly, the catalysts proposed through the optimization process were localized in the lower-left region of the 2-D plane, corresponding to superior performance (i.e., lower HER overpotential), as shown in Figure 3b,e. After the second round of optimization, the newly suggested catalysts were distributed more narrowly in this region (Figure 3c,f). During the optimization process, the BO

© 2025 The Author(s). Advanced Functional Materials published by Wiley-VCH GmbH

16163028, 0, Downloaded from https://advanced.onlinelibrary.wiley.com/doi/10.1002/adfm.202424887 by Junhyeok Seo - Gwangju Institute Of Science And Technology (Gist) , Wiley Online Library on [18/03/2025]. See the Terms and Conditions (https://onlinelibrary.wiley.com/terms-and-conditions) on Wiley Online Library for rules of use; OA articles are governed by the applicable Creative Commons License

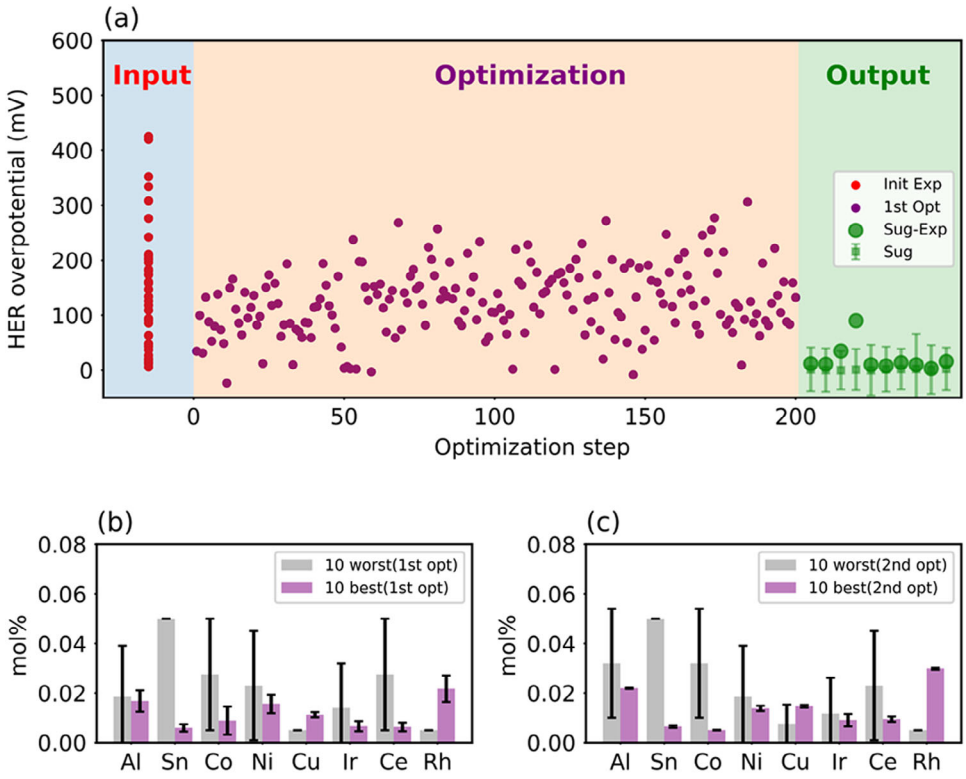

Figure 4. a) One optimization round. Red circle: initial training data; purple circle: suggested catalyst from each step; green square: suggested best catalyst; green circle: experimental result with the suggested best catalyst. In practice, the 200-step optimization (orange region in Figure 4) was independently repeated 10 times, with one catalyst composition proposed from each optimization. Element composition of 10 best (low HER overpotential) and worst (high HER overpotential) catalysts b) in 1st optimization round and c) 2nd optimization round. Error bars shown in all panels represent the standard deviation.

algorithm navigated the composition space using predictions from the GPR model, identifying catalyst compositions with the potential to reduce HER overpotential. The optimization demonstrated convergence by the two rounds, indicating that additional iterations were unnecessary. While a comprehensive exploration of the composition space could potentially identify novel catalysts with enhanced activity, the associated computational and experimental costs were deemed prohibitive. As a result, the optimization was concluded after the second round in this study.

Throughout the BO process, the GPR model was employed to predict the performance of hypothetical catalyst compositions. To assess whether the optimizer adequately explored the specified composition space, the compositions and performance of catalysts examined during one optimization round were analyzed (**Figure 4**). At the beginning of optimization, the training data ("Input" in Figure 4a) comprised 50 catalysts spanning a range of HER overpotentials. Red circles in Figure 4a represent the compositions and experimental performance of these catalysts. BO was performed based on these training data points, with the pre-trained GPR model predicting the performance of proposed catalysts ("Optimization" in Figure 4a). The purple points in Figure 4a indicate the compositions suggested during 200 optimization steps, reflecting the predictions made by the GPR model. In the proposal and validation stage ("Output" in Figure 4a), the catalyst with the best predicted performance among the 200 proposed compositions (green square) was selected, and its actual performance was confirmed experimentally (green circle). Most of the proposed catalysts were well within the standard deviation predicted by GPR. However, a catalyst falls outside this range and in the range of about two times the standard deviation. By including this data in the training data, the GPR model can predict this data accurately in the next round of BO. By comparing the top 10 and bottom 10 catalyst compositions in terms of HER overpotential within a single optimization round (Figure 4b,c), it was evident that a wide range of compositions had been explored. Additionally, catalysts proposed during the optimization process generally exhibited good experimental performance, demonstrating the effectiveness of the BO approach in conjunction with the GPR model.

2.2. Experimental Validation of Optimal HENPs

Upon completing all iterations, the optimal composition of the octonary HENP catalyst was identified, exhibiting an exceptionally low HER overpotential of 0.007 mV (Table S4, Supporting Information). This composition was further validated experimentally. The electrocatalytic activity and stability of the HENPs for HER were evaluated in a three-electrode configuration through a series of electrochemical tests and compared with the

© 2025 The Author(s). Advanced Functional Materials published by Wiley-VCH GmbH

16163028, 0, Downloaded from https://advanced.onlinelibrary.wiley.com/doi/10.1002/adfm.202424887 by Junhyeok Seo - Gwangju Institute Of Science And Technology (Gist) , Wiley Online Library on [18/03/2025]. See the Terms and Conditions (https://onlinelibrary.wiley.com/terms-and-conditions) on Wiley Online Library for rules of use; OA articles are governed by the applicable Creative Commons License

commercial Pt/C. Linear sweep voltammetry (LSV) curves of HENPs and Pt/C in 1M KOH alkaline electrolyte (pH 13.9) at a scan rate of 2 mV s^{-1} are presented in **Figure 5a**. The LSV curves, recorded without iR-compensation and normalized to a geometric surface area of 1 cm^2, revealed that HENPs achieved a low overpotential (η) of 12 mV at a current density of 10 mA cm^{-2}, which is lower than Pt/C (η_{10} = 16 mV). At higher current densities (50, 100, 150, and 200 mA cm^{-2}), the HENP electrodes required overpotentials of 76, 147, 249, and 290 mV versus RHE, respectively, all of which were lower than those required by Pt/C (Figure S8, Supporting Information). Additionally, the HENPs outperformed other recently reported high-entropy and precious metal-based HER electrocatalysts (Figure 5j; Table S5, Supporting Information). HER-LSV curve of HENPs measured in a three-electrode setup using Hg/HgO reference electrode, graphite rod counter electrode in 1 M KOH solution is provided in Figure S9 (Supporting Information). No overpotential change was observed at 10 mA cm^{-2}, although a slight difference in current density was noted at higher negative potentials. To further understand the electrochemical behavior of HENPs, Tafel plots were analyzed (Figure 5b). The HENPs exhibited a Tafel slope of 34.7 mV dec^{-1}, indicating the Volmer–Heyrovsky mechanism governs the HER.[47] This Tafel slope was much lower than that of Pt/C (36.1 mV dec^{-1}), suggesting more efficient hydrogen desorption on HENP catalyst surface.

For the OER, the optimal HENP composition demonstrated a remarkably low overpotential of 213.06 mV (Table S3, Supporting Information), which was also validated experimentally. The OER activity and stability of HENPs were compared with those of commercial IrO_2. Figure 5c shows the OER-LSV curves of HENPs and IrO_2 in 1M KOH alkaline electrolyte at a scan rate of 2 mV s^{-1}. Reverse LSV scans were employed to minimize interference from oxidation peaks of metal ions. The HENPs demonstrated superior OER catalytic activity, achieving an overpotential of 239 mV at 10 mA cm^{-2} (without iR correction), far surpassing IrO_2 (311 mV) and other recently reported catalysts (Figure 5k; Table S6, Supporting Information). The experimentally validated results closely matched those predicted by the BO method, with minor deviations attributed to electrode resistance. The OER kinetics were further analyzed using Tafel plots (Figure 5d). The HENPs exhibited a low Tafel slope of 44 mV dec^{-1}, significantly smaller than IrO_2 (81 mV dec^{-1}), indicating that the rate-determining step involves hydroxyl intermediate formation ($MO + OH^- \rightarrow MOOH + e^-$).[48]

The electrochemical surface area (ECSA) of the HENPs was determined using the double-layer capacitance (C_{dl}) method, based on cyclic voltammetry (CV) measurements in the non-Faradaic region at varying scan rates (Figure S10, Supporting Information). As shown in Figure 5e, the C_{dl} of HENPs (24.12 mF cm^{-2}) surpassed that of IrO_2 (19.18 mF cm^{-2}), corresponding to ECSA values of 962.7 and 776.5, respectively (Figure S11, Supporting Information). The superior ECSA of HENPs is attributed to their ultra-small particle size, abundant reactive sites, and high surface exposure. Intrinsic catalytic activity was assessed through turnover frequency (TOF), calculated from the equation, TOF (s^{-1}) = (J × A)/(F × 2 × n),[49] where, J is the current density (mA/cm^2), A is the area (cm^2), F is the Faraday constant and n is the number of moles of elements, calculated on the basis of the weight of the catalyst loading on the electrode surface. The TOF values of HENPs exceeded those of Pt/C and IrO_2 across various reduction and oxidation potentials (Figure S12a,b, Supporting Information), attributed to the synergistic effects among constituent atoms and optimized adsorption strength of intermediates.[50] Charge transfer resistance (R_{ct}) was evaluated via Nyquist plots, fitted by the capacitance-resistance circuit (Figure 5f), under a positive potential of 0.5 V with the frequency range of 0.1 to 10^5 Hz. The HENPs exhibited a lower R_{ct} (2.65 Ω) compared to IrO_2 (3.22 Ω), indicating faster OER kinetics at the electrode–electrolyte interface. The presence of two semicircles in the Nyquist plot suggested mixed states involving both metals and oxides.[51] The stability of HENPs was assessed using chronopotentiometry under HER and OER conditions at 10 mA cm^{-2} for 25 h (Figure 5g). The HENPs maintained consistent performance throughout, with no notable loss in HER overpotential and minimal OER overpotential loss (≈0.01 V). The LSV curves before and after stability testing are shown in Figure S13 (Supporting Information). To evaluate overall water-splitting performance, an alkaline electrolyzer was assembled using HENPs as both the anode and cathode. The electrolyzer required a remarkably low cell voltage of 1.48 V (total overpotential of 0.25 V) to achieve 10 mA cm^{-2}, outperforming the Pt/C||IrO_2 reference (1.59 V; Figure 5h). Furthermore, the electrolyzer demonstrated excellent durability over 15 days of operation (Figure 5i).

2.3. Characterization of Optimal HENPs

The particle size and microstructure of the HENPs were characterized using high-resolution transmission electron microscopy (HR-TEM) (**Figure 6a–c**). The analysis revealed ultra-small nanoparticles uniformly distributed without noticeable aggregation (Figure 6a). A statistical analysis of fifty randomly selected nanoparticles indicated a mean size of ≈2.02 nm, with a narrow size distribution (Figure 6a inset). This particle size is significantly smaller than those reported for other high-entropy catalysts (Tables S5 and S6, Supporting Information). The surface area was found to exhibit a linear correlation with the inverse of particle size, emphasizing the critical role of controlled size in catalytic reaction kinetics. Previous studies have shown that particle sizes below 5 nm can induce substantial changes in catalytic behavior.[52] High-magnification HR-TEM images (Figure 6b) displayed distinct lattice fringes with interplanar spacings of 0.22 nm and 0.19 nm, corresponding to the (111) and (200) facets of face-centered cubic (FCC) high-entropy nanoparticles.[53] Selected area diffraction pattern (SAED) patterns (Figure 6c) exhibited diffraction rings with discrete spots, confirming the crystallinity of the nanoparticles, and the diffraction rings were indexed to the (111), (200), and (220) planes of the FCC structure.

The powder X-ray diffraction (PXRD) pattern (Figure 6d) further corroborated the TEM findings, displaying broad diffraction peaks at 40.9°, 52.98°, and 69.15°, corresponding to the (111), (200), and (220) planes of FCC-structured HENPs.[54,55] The absence of distinct metallic peaks confirmed the successful formation of high-entropy nanoparticles. Energy-dispersive spectroscopy (EDS) mapping and line scanning profiles (Figure 6e–n; Figure S14, Supporting Information) revealed a uniform distribution of all constituent elements throughout the nanoparticles,

© 2025 The Author(s). Advanced Functional Materials published by Wiley-VCH GmbH

16163028, 0, Downloaded from https://advanced.onlinelibrary.wiley.com/doi/10.1002/adfm.202424887 by Junhyeok Seo - Gwangju Institute Of Science And Technology (Gist) , Wiley Online Library on [18/03/2025]. See the Terms and Conditions (https://onlinelibrary.wiley.com/terms-and-conditions) on Wiley Online Library for rules of use; OA articles are governed by the applicable Creative Commons License

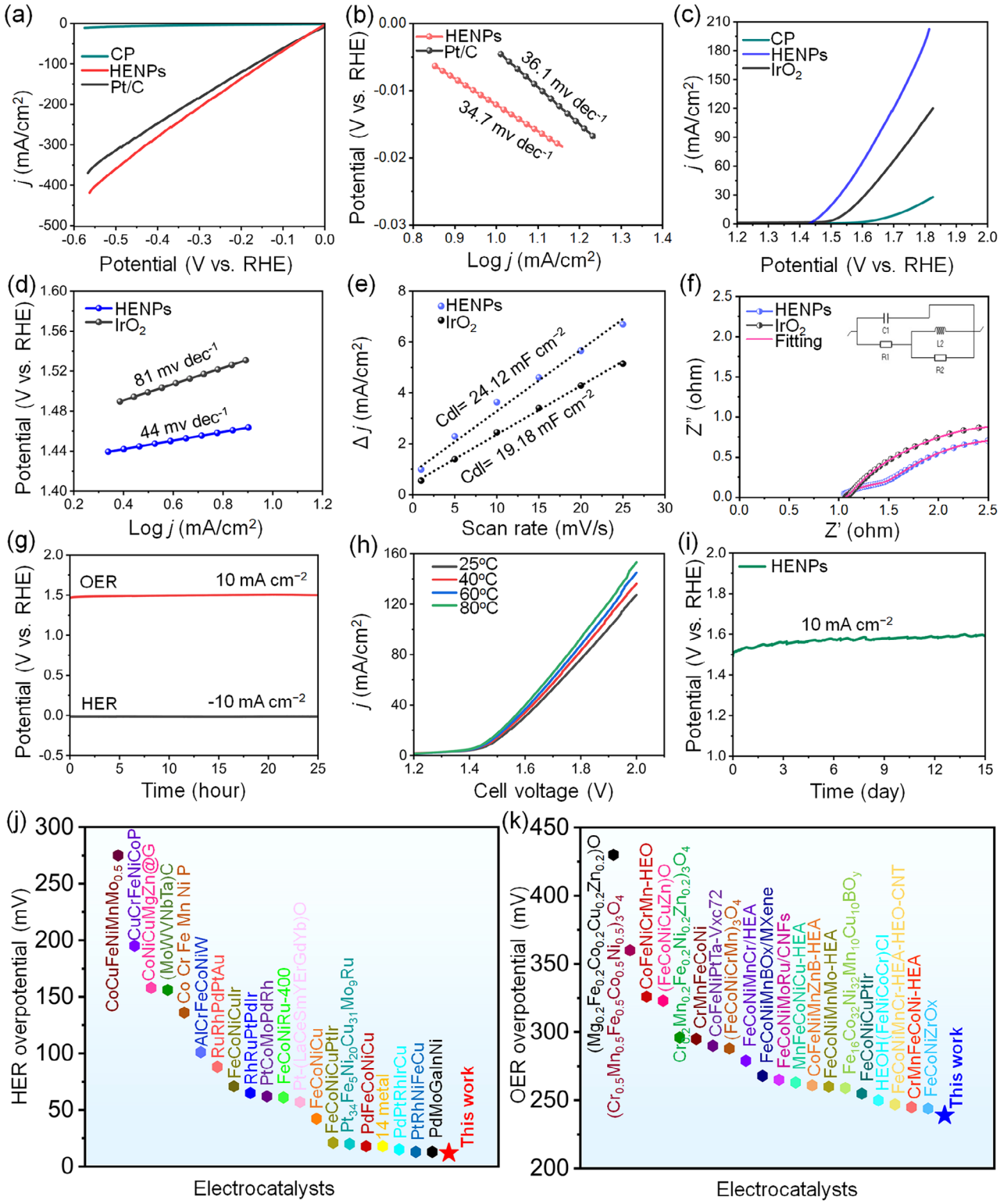

Figure 5. a) HER-LSV curves of HENPs, and Pt/C in 1 M KOH solution, b) corresponding HER Tafel plots, c) OER-LSV curves of HENPs, and IrO_2 in 1 M KOH solution, d) corresponding OER Tafel plots, e) current density difference plotted against scan rates and the estimation of C_{dl} f) Nyquist plots of HENPs and IrO_2, g) chronopotentiometry of HENPs at a constant current density of 10 mA cm^{-2} for 24 h. h) LSV polarization curve of HENPs electrodes for overall water splitting reaction in a two-electrode configuration, i) long-term durability test at a current density of 10 mA/cm^2 for 15 days, j) comparison of HER overpotential with recent reports in alkaline electrolyte. k) comparison of OER overpotential with recent reports in alkaline electrolyte.

© 2025 The Author(s). Advanced Functional Materials published by Wiley-VCH GmbH

16163028, 0, Downloaded from https://advanced.onlinelibrary.wiley.com/doi/10.1002/adfm.202424887 by Junhyeok Seo - Gwangju Institute Of Science And Technology (Gist) , Wiley Online Library on [18/03/2025]. See the Terms and Conditions (https://onlinelibrary.wiley.com/terms-and-conditions) on Wiley Online Library for rules of use; OA articles are governed by the applicable Creative Commons License

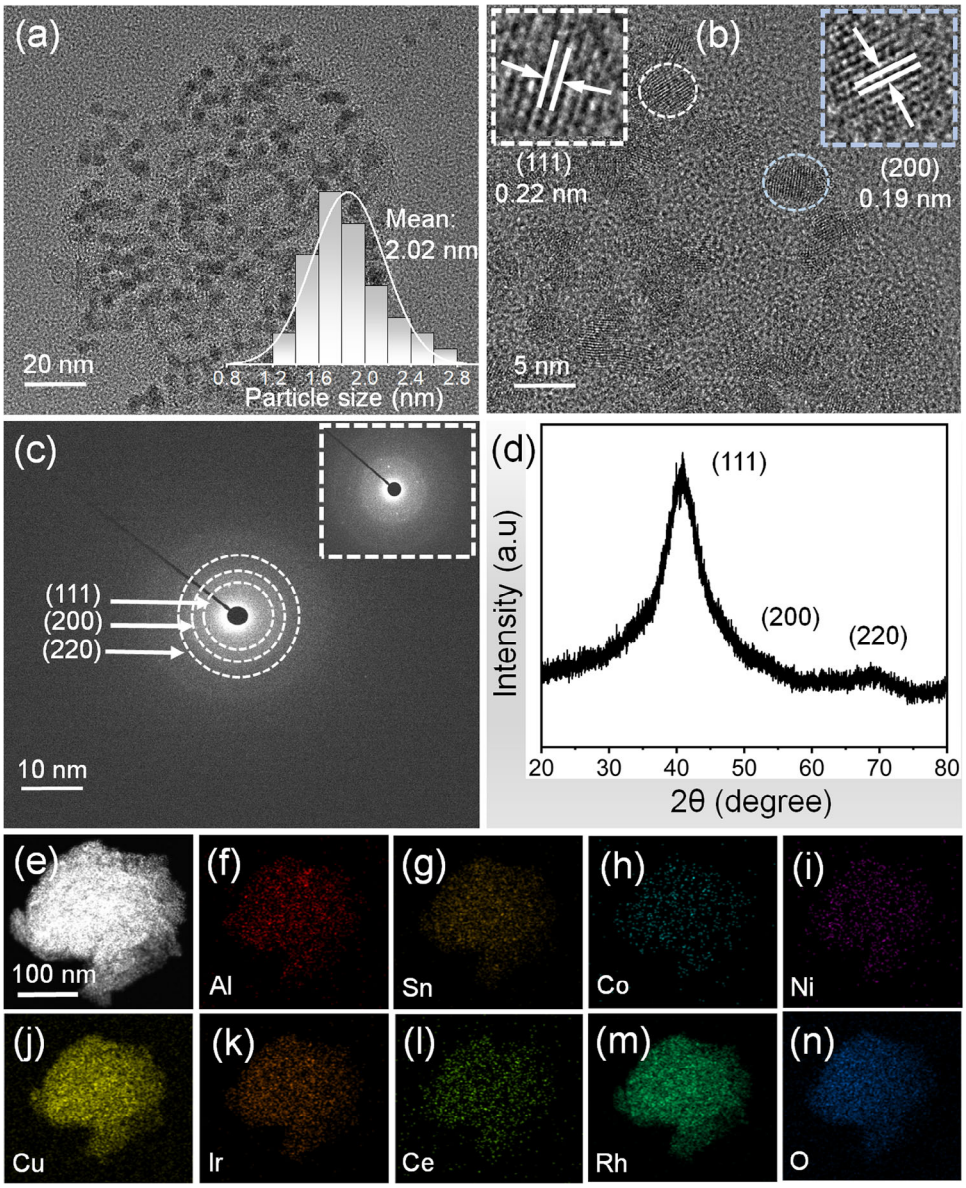

Figure 6. a) HR-TEM image of synthesized HENPs (insert: histogram for nanoparticle size distribution). b) High magnification HR-TEM image of HENPs with diffraction plane analysis. c) SAED pattern of HENPs (insert: zoomed in version), d) PXRD pattern of HENPs, e–n) element mappings of HENPs.

indicating effective atomic mixing and the formation of a high-entropy structure. The presence of uniformly distributed oxygen was also detected, prompting the use of Raman spectroscopy to evaluate metal-oxide bonds. Raman spectra (Figure S15, Supporting Information) showed a characteristic peak at 561 cm^{-1}, attributed to the M-O stretching vibration of high-entropy oxide (HEO) nanoparticles.[56] The absence of peaks corresponding to individual metal oxides suggested the formation of a combined HEA-HEO heterostructure.

X-ray photoelectron spectroscopy (XPS) was employed to investigate the surface chemical states of the HENPs's elements. A survey scan spectrum confirmed the presence of Al, Sn, Co, Ni, Cu, Ir, Ce, Rh, and O (Figure S16, Supporting Information). High-resolution spectra provided further information of each elements' oxidation states: Al 2*p*: Peaks at 72.7 and 74.2 eV correspond to Al^0 and Al^{3+} states, respectively (Figure S17a, Supporting Information).[57] Sn 3*d*: Peaks at 485.2 and 493.6 eV correspond to Sn^0, while 486.3 and 494.7 eV indicate Sn^{4+} state (Figure S17b, Supporting Information).[58] The lower contents of Al^0 and Sn^0 states compared to the Al^{3+} and Sn^{2+} states are due to their high reducing activity.[59] Co 2*p*: Peaks at 778.2, 779.7, and 784.1 eV correspond to Co^0, Co^{2+}, and satellite peak, respectively (Figure S17c, Supporting Information). Ni 2*p*: Peaks at 852.6, 856.8, and 866.1 correspond to Ni^0, Ni^{2+}, and satellite peak, respectively (Figure S17d, Supporting Information). Cu 2*p*: Peaks at 931.1 and 933.5 eV correspond to Cu^0 and Cu^{2+}, respectively (Figure S17e, Supporting Information).[60] Ir 4*f*: Peaks at 60.7 and

© 2025 The Author(s). Advanced Functional Materials published by Wiley-VCH GmbH

16163028, 0, Downloaded from https://advanced.onlinelibrary.wiley.com/doi/10.1002/adfm.202424887 by Junhyeok Seo - Gwangju Institute Of Science And Technology (Gist) , Wiley Online Library on [18/03/2025]. See the Terms and Conditions (https://onlinelibrary.wiley.com/terms-and-conditions) on Wiley Online Library for rules of use; OA articles are governed by the applicable Creative Commons License

63.9 eV correspond to Ir^0, while peaks at 62.1 and 65.3 eV indicate Ir^{4+} (Figure S17f, Supporting Information). Ce 3*d*: Peaks at 882.9, 885.7, and 889.7 eV correspond to Ce^{4+}, Ce^{3+}, and satellite peak, respectively, with no metallic Ce observed due to its high oxidation potential (Figure S17g, Supporting Information).[61] Rh 3*d*: Peaks at 307.1 and 311.5 correspond to Rh^0, while 308.2 and 312.7 eV correspond to Rh^{3+}, along with satellite peaks at 309.7 and 314.1 eV (Figure S17h, Supporting Information).[62] O 1*s*: Peaks at 529.6, 530.4, and 532.7 eV were attributed to M-O, M-OH, and adsorbed water, respectively (Figure S17I, Supporting Information).

The XPS findings highlighted strong oxidation peaks for Ce, Al, and Sn, consistent with their high electropositive and oxophilic nature.[63] Their position at the lower end of the Ellingham diagram confirms their high oxidation potential, with an inclination to their oxide formation.[64] Conversely, Ir, Rh, Co, Ni, and Cu exhibited pronounced metallic peaks, aligning with their high reduction potentials and positions at the upper end of the Ellingham diagram. Together, these results confirmed the HEA-HEO heterostructure of the synthesized HENPs. Similar analyses were performed for HENPs optimized for OER (Figure S18, Supporting Information). These nanoparticles exhibited a particle size of 1.85 nm (Figure S18a, Supporting Information). The SAED and XRD patterns (Figure S18c,d, Supporting Information) confirmed the high-entropy structure plane orientation, while EDS mapping showed uniform element distribution (Figure S18e,n, Supporting Information). XPS analysis revealed trends similar to the HER-optimized HENPs, with strong oxidation peaks for Ce, Al, and Sn, and metallic peaks for Ir, Rh, Co, Ni, and Cu (Figure S19a–I, Supporting Information).

To understand the improved performance of the HER catalyst found in this work, additional DFT calculations were performed and several adsorption sites were compared in terms of the hydrogen adsorption free energy. Due to the intrinsic complexity of HENPs, not all adsorption sites were considered in the DFT calculations. As shown in Figure S20 (Supporting Information), the DFT results showed that Rh site was considered as the most promising site for HER, which was consistent with the experimental findings. Among other surface atoms, Ir and Sn sites could be involved in HER. To determine the effect of the microenvironment, the hydrogen adsorption free energy was calculated for three Rh atoms on the surface. The results showed that the environment can change the free energy by ≈ 0.2 eV (Figure S21, Supporting Information). Therefore, it was concluded that the enhanced performance observed in HENPs was primarily due to the presence of Rh sites modulated by the microenvironment of other elements. The effect of the other elements in the detailed calculations will be an interesting topic for future research.

The dissolution of metal elements during electrochemical testing under alkaline conditions is indeed a valid concern. We performed TEM analysis to examine the morphological and structural changes in the HENPs catalyst after HER and OER stability. Figure S22a–d (Supporting Information) presents the HR-TEM images of HENPs after 25 h of HER/OER stability testing. No significant changes in morphology were observed; however, nanoparticle aggregation was noted, particularly after the OER stability test, which is expected under harsh alkaline conditions.[65,66] Despite this, the results confirm the structural stability of the synthesized HENPs catalyst. To further investigate the atomic ratio of elements before and after the stability tests, XPS analysis was conducted. Table S8 (Supporting Information) provides the elemental composition information of the HENPs catalysts before and after stability tests. While some degree of elemental dissolution occurred during the electrochemical tests, all elements were still detectable after the stability tests. For HER, rhodium exhibited slight dissolution, indicating its role as a prominent active site for the HER reaction. For OER, aluminum and tin displayed higher dissolution levels after the stability tests, highlighting their susceptibility to dissolution under prolonged OER operations.

From our findings, the synthesized HENPs exhibit excellent HER and OER activities. However, the ML model showed limitations for OER catalysts due to the dynamic catalytic activation process occurring in situ during water oxidation, which disrupts the simple relationship between the chemical composition of HENPs and their catalytic performance. DFT calculations revealed that Rh is a key contributor to active sites for HER, and the electronic structure modulations by neighboring atoms further enhance HER activity. The stability of HENPs under HER and OER conditions is influenced by the leaching of certain elements, such as Al and Sn, in harsh alkaline media. This insight suggests strategies to enhance stability, such as immobilizing HENPs on stable supports or alloying with more corrosion-resistant elements. Additionally, nanoparticle aggregation observed after prolonged testing emphasizes the need to optimize particle size and distribution to maintain structural integrity during electrochemical reactions. The ML approach not only accelerates the screening process but also provides valuable insights into key factors such as metal ratios that affect catalytic activity and stability. Furthermore, other factor including particle size, crystal facets, strain effects, and structural evolution during electrochemical reactions significantly influence HER/OER performance.[67–69] These aspects are critical for designing highly efficient HER/OER electrocatalysts, and future research will focus on these areas in greater detail.

3. Conclusion

A catalyst-discovery framework was developed by integrating an active learning model with Bayesian Optimization (BO) to efficiently explore the extensive compositional space of octonary high-entropy nanoparticles (HENPs) for hydrogen and oxygen evolution reactions (HER and OER). This framework enabled dynamic, user-guided interaction with machine learning, facilitating systematic convergence toward optimal compositions while minimizing experimental data requirements. Precursor mixture composition served as the primary input, supported by a high-throughput experimental dataset. Gaussian Process Regression (GPR) surrogate models were utilized for rapid prediction of target properties, while SHAP analysis and the t-SNE method provided insights into composition-property relationships. Through BO, 10 promising HENP compositions were identified and experimentally evaluated. The optimized HER catalyst demonstrated an exceptionally low overpotential of 12 mV, while the OER catalyst exhibited an overpotential of 239 mV at a current density of 10 mA/cm^2, outperforming commercial Pt/C and IrO_2 catalysts, respectively. For HER, the framework successfully enhanced catalytic performance within the

© 2025 The Author(s). Advanced Functional Materials published by Wiley-VCH GmbH

16163028, 0, Downloaded from https://advanced.onlinelibrary.wiley.com/doi/10.1002/adfm.202424887 by Junhyeok Seo - Gwangju Institute Of Science And Technology (Gist) , Wiley Online Library on [18/03/2025]. See the Terms and Conditions (https://onlinelibrary.wiley.com/terms-and-conditions) on Wiley Online Library for rules of use; OA articles are governed by the applicable Creative Commons License

16163028, 0, Downloaded from https://advanced.onlinelibrary.wiley.com/doi/10.1002/adfm.202424887 by Junhyeok Seo - Gwangju Institute Of Science And Technology (Gist) , Wiley Online Library on [18/03/2025]. See the Terms and Conditions (https://onlinelibrary.wiley.com/terms-and-conditions) on Wiley Online Library for rules of use; OA articles are governed by the applicable Creative Commons License

prediction uncertainty of the machine learning model. However, for OER, the quality of the initial machine learning model was insufficient, and limitations in the approach were observed. The limitation is attributed to the dynamic catalytic activation process occurring in situ during water oxidation, which disrupt the linear relationship between the chemical composition of HENPs and their catalytic performance. For OER, simplifying the catalytic material is necessary, but this poses challenges in securing the extensive amount of data required for machine learning, thereby limiting the application of this method. At present, enhancing the efficiency of OER has been achieved primarily through catalyst design based on human intuition. This study demonstrates the potential of AI-assisted catalyst development for hydrogen evolution reaction while also addressing its limitations for more complex reactions like oxygen evolution reaction. These findings provide a foundation for further refinement of machine learning frameworks and suggest directions for integrating human expertise with data-driven methodologies in catalyst discovery.

4. Experimental Section

Ultrasmall High Entropy Nanoparticles(HENPs) Synthesis: All chemicals were purchased from Sigma-Aldrich. Eight different metal precursors–$AlCl_3$ (anhydrous), $SnCl_2.2H_2O$, $CoCl_2.6H_2O$, $NiCl_2.6H_2O$, $CuCl_2$ (anhydrous), $IrCl_3.xH_2O$, $CeCl_3.7H_2O$, and $RhCl_3{\cdot}xH_2O$–were dissolved in 50 ml deionized (DI) water. Separately, 0.55 mg of poly(N-vinyl-2-pyrrolidone) (PVP) and 0.2 g of $NaBH_4$ were dissolved in 150 mL of triethylene glycol (TEG). The metals precursor solution was added dropwise into the preheated TEG solution at 230 °C under stirring for 2 h, then allowed to cool. The octonary AlSnCoNiCuIrCeRh HENPs were separated via centrifugation with acetone and washed with ethanol and DI water several times to remove excess PVP. The resultant black powder was dried in a vacuum oven at 60 °C. To construct the dataset for exploring the optimal composition, molar concentrations of the metal precursors were randomly selected, as detailed in Table S1 (Supporting Information).

Characterization: The crystal structure and phase formation of the catalysts were analyzed using a powder X-ray diffractometer (PXRD; Smart lab, Rigaku) equipped with a Cu$K\alpha$ radiation emitter (9 kW) and a PIXcel^{2D} detector, operating at 40 kV and 30 mA. The high-entropy structure and ultrasmall particle size were observed using a high-resolution, double-Cs-corrected transmission electron microscope (HR-TEM, JEM-ARM300F2, JEOL) coupled with an energy-dispersive X-ray spectroscopy (EDS) analyzer, operated at 300 kV. Elemental mapping was performed using an 80 keV JEM ARM 200F equipped with a spherical aberration corrector. Surface composition and electronic states of the HENPs were investigated using high-resolution X-ray photoelectron spectroscopy (XPS; NEXSA, Thermo Fisher Scientific) with Al$K\alpha$ radiation and a 128-Channel detector.

Electrochemical Analysis: Electrochemical measurements were conducted at room temperature using a Gamry Interface 1010 potentiostat/galvanostat/ZRA. A three-electrode setup was used, with a Pt wire as the counter electrode, an Ag/AgCl electrode saturated with KCl as the reference, and the synthesized HENPs on carbon paper (CP, surface area = 1 cm^2) as the working electrode. Catalytic ink was prepared by dispersing 10 mg of the synthesized HENPs in 950 µL of isopropyl alcohol and 50 µL of Nafion solution. A 20 µL aliquot of the ink was coated onto a cleaned CP surface (loading mass = 0.2 mg cm^{-2}) using a micro-syringe, and the CP was dried at 80 °C for 2 h. A similar procedure was used to prepare Pt/C and IrO_2 electrodes for comparison.

Catalytic activities were evaluated using linear sweep voltammetry (LSV) at a scan rate of 10 mV s^{-1} in 1 M KOH (pH 13.9) electrolyte. Potentials measured against Ag/AgCl were converted to potentials versus RHE using the Nernst equation ($E_{RHE} = E_{Ag/AgCl} + 0.197 + 0.05916 \times pH$). Electrochemical impedance spectroscopy was conducted over a frequency range of 10^{-2} to 10^5 Hz, applying potentials of 1.52 V versus RHE. The electrochemically active surface area (ECSA) was estimated by calculating the electrochemical double-layer capacitance (C_{dl}) in a non-Faradaic potential region. Cyclic voltammetry (CV) was conducted at scan rates of 1, 5, 10, 15, 20, and 25 mV s^{-1}. Current density differences (ΔI) were plotted against scan rates to determine $2C_{dl}$, where $2C_{dl} = d(\Delta I)/dv$. Electrochemical stability was assessed using chronopotentiometry under constant current densities of −10 mA/cm^2 (for HER) and 10 mA/cm^2 (for OER). Overall water-splitting performance was evaluated in a two-electrode setup with 1 M KOH electrolyte.

Machine Learning (ML) and Bayesian Optimization (BO): A framework combining machine learning (ML) and Bayesian optimization (BO) was developed to explore the optimal composition of catalysts containing 8 metal elements (Al, Sn, Co, Ni, Cu, Ir, Ce, and Rh). Initially, 50 experimental data points were generated by randomly selecting molar concentrations of the elements, with HER and OER activities evaluated experimentally. The results were included in the initial dataset. The input variable for the ML models was the precursor ratio used in HENP synthesis. The output or target variable was the measured HER/OER overpotential for each HENP composition. These experimental results were incorporated into internal Gaussian Process Regression (GPR) models within the BO code. The list of hyperparameters used in this study was tabulated in the Table S7 (Supporting Information). The first round of BO used the entire experimental dataset to train the GPR model, followed by 200 iterations using the upper confidence bound (UCB) acquisition function. With the UCB acquisition function, the prediction uncertainty estimated from the GPR model was considered in the BO. This approach identified catalyst compositions predicted to exhibit optimal performance. By varying the random number seed, 10 new catalyst compositions were suggested for experimental validation. For HER, novel compositions not included in the training data were identified, whereas for OER, the suggested compositions were similar to the best catalysts in the training data. Thus, a second round of BO was conducted to improve only the HER activity. This iteration used an expanded dataset of 60 experimental data points. Performance improvements after the second round were marginal, indicating convergence of the BO process. The BO code is publicly available at our GitHub repository (https://github.com/hwk-grp/BO_HENPs).

Statistical Analysis: The GPR model is basically based on a Gaussian distribution and provides both predicted values and associated uncertainty. In this work, the GPR model was used as implemented in the Scikit-learn library[70] and the uncertainty was expressed in terms of standard deviation (SD). All results obtained with the GPR model were presented as mean ± SD. Surrogate models for BO were compared using leave-one-out cross-validation. It appears that a histogram analysis was used to show the particle size distribution of HENPs, which is a common statistical analysis among experimentalists.

Supporting Information

Supporting Information is available from the Wiley Online Library or from the author.

Acknowledgements

S.P. and D.B.H. contributed equally. This work was supported by the National Research Foundation of Korea (NRF) grant funded by the Korean government (RS-2021-NR060081), the GIST Research Project grant funded by the GIST in 2024, and the Competitiveness Reinforcement Project for Industrial Clusters funded by the Korea Industrial Complex Corporation (HGGJ2302).

Conflict of Interest

The authors declare no conflict of interest.

© 2025 The Author(s). Advanced Functional Materials published by Wiley-VCH GmbH

Data Availability Statement

The data that support the findings of this study are available in the supplementary material of this article.

Keywords

active learning, Bayesian optimization, high entropy nanoparticles, hydrogen evolution reaction, oxygen evolution reaction

Received: December 17, 2024
Revised: February 21, 2025
Published online:

[1] X. Yan, Y. Zhou, S. Wang, *Adv. Funct. Mater.* **2024**, *35*, 2413115.
[2] Z. Wang, X. Tan, Z. Ye, S. Chen, G. Li, Q. Wang, S. Yuan, *Green Chem.* **2024**, *26*, 9569.
[3] X. Zou, J. Xie, Z. Mei, Q. Jing, X. Sheng, C. Zhang, Y. Yang, M. Sun, F. Ren, L. Wang, T. He, *Proc. Natl. Acad. Sci. USA* **2024**, *121*, 2313239121.
[4] W. L. Hsu, C. W. Tsai, A. C. Yeh, J. W. Yeh, *Nat. Rev. Chem.* **2024**, *8*, 471.
[5] T. A. Batchelor, J. K. Pedersen, S. H. Winther, I. E. Castelli, K. W. Jacobsen, J. Rossmeisl, *Joule* **2019**, *3*, 834.
[6] J. Kwon, S. Sun, S. Choi, K. Lee, S. Jo, K. Park, Y. K. Kim, H. B. Park, H. Y. Park, J. H. Jang, H. Han, *Adv. Mater.* **2023**, *35*, 2300091.
[7] B. K. Hamzah, J. Zhang, Y. Liang, Y. Wei, Y. Z. Huang, *J. Mater. Chem. A.* **2024**, *12*, 9961.
[8] A. Poonia, M. Kishor, K. P. R. Ayyagari, *Sci. Rep.* **2024**, *14*, 7692.
[9] W. Xu, E. Diesen, T. He, K. Reuter, J. T. Margraf, *J. Am. Chem. Soc.* **2024**, *146*, 7707.
[10] V. A. Mints, K. L. Svane, J. Rossmeisl, M. Arenz, *ACS Catal.* **2024**, *14*, 6936.
[11] M. Kim, Y. Kim, M. Y. Ha, E. Shin, S. J. Kwak, M. Park, I. D. Kim, W. B. Jung, W. B. Lee, Y. Kim, H. T. Jung, *Adv. Mater.* **2023**, *35*, 2211497.
[12] L. Cheng, Y. Tang, K. Ostrikov, Q. Xiang, *Angew. Chem.* **2024**, *63*, 202313599.
[13] M. Karthikeyan, D. M. Mahapatra, A. S. A. Razak, A. A. Abahussain, B. Ethiraj, L. Singh, *Catal. Rev.* **2024**, *66*, 997.
[14] J. Benavides-Hernández, F. Dumeignil, *ACS Catal.* **2024**, *14*, 11779.
[15] A. P. Dmitrieva, A. Fomkina, C. Tracey, A. Ayati, E. Romanenko, P. Krivoshapkin, E. F. Krivoshapkina, *J. Mater. Chem. A.* **2024**, *12*, 31074.
[16] B. M. Abraham, M. V. Jyothirmai, P. Sinha, F. Viñes, J. K. Singh, F. Illas, *Comput. Mol. Sci.* **2024**, *14*, e1730.
[17] C. Sun, R. Goel, A. R. Kulkarni, *Langmuir* **2024**, *40*, 3691.
[18] J. K. Pedersen, C. M. Clausen, O. A. Krysiak, B. Xiao, T. A. Batchelor, T. Löffler, V. A. Mints, L. Banko, M. Arenz, A. Savan, W. Schuhmann, *Angew. Chem.* **2021**, *133*, 24346.
[19] K. L. Svane, J. Rossmeisl, *Angew. Chem.* **2022**, *134*, 202201146.
[20] W. T. Hong, R. E. Welsch, Y. Shao-Horn, *J. Phys. Chem. C.* **2016**, *120*, 78.
[21] P. Raccuglia, K. C. Elbert, P. D. Adler, C. Falk, M. B. Wenny, A. Mollo, M. Zeller, S. A. Friedler, J. Schrier, A. J. Norquist, *Nature* **2016**, *533*, 73.
[22] G. Smith, E. J. Dickinson, *Nat. Commun.* **2022**, *13*, 6832.
[23] D. Khatamsaz, B. Vela, P. Singh, D. D. Johnson, D. Allaire, R. Arróyave, *Npj Comput. Mater.* **2023**, *9*, 49.
[24] Z. Rao, P. Y. Tung, R. Xie, Y. Wei, H. Zhang, A. Ferrari, T. P. C. Klaver, F. Körmann, P. T. Sukumar, A. Kwiatkowski da Silva, Y. Chen, *Science* **2022**, *378*, 78.
[25] X. Li, Y. Che, L. Chen, T. Liu, K. Wang, L. Liu, H. Yang, E. O. Pyzer-Knapp, A. I. Cooper, *Nat. Chem.* **2024**, *16*, 1286.
[26] J. Oh, J. Lee, J. Park, N. Jeon, G. S. Na, H. Chang, J. Huh, H. W. Kim, Y. Yun, *ACS Mater. Lett.* **2024**, *6*, 5138.
[27] K. J. Jenewein, L. Torresi, N. Haghmoradi, A. Kormányos, P. Friederich, S. Cherevko, *J. Mater. Chem. A.* **2024**, *12*, 3072.
[28] L. Banko, O. A. Krysiak, J. K. Pedersen, B. Xiao, A. Savan, T. Löffler, S. Baha, J. Rossmeisl, W. Schuhmann, A. Ludwig, *Adv. Energy Mater.* **2022**, *12*, 2103312.
[29] J. Yang, Z. Wang, X. Zhang, X. Zhang, B. Niu, C. Wang, C. Du, J. He, B. Shan, Q. Li, *Chem. Eng. J.* **2024**, *493*, 52300.
[30] M. Kim, Y. Kim, M. Y. Ha, E. Shin, S. J. Kwak, M. Park, I. D. Kim, W. B. Jung, W. B. Lee, Y. Kim, H. T. Jung, *Adv. Mater.* **2023**, *35*, 2211497.
[31] W. Xu, E. Diesen, T. He, K. Reuter, J. T. Margraf, *J. Am. Chem. Soc.* **2024**, *146*, 7698.
[32] J. Fu, A. Kumar, O. Nachum, G. Tucker, S. Levine, Arxiv 2004.07219**2020**.
[33] P. C. Jennings, S. Lysgaard, J. S. Hummelshøj, T. Vegge, T. Bligaard, *Npj Comput. Mater.* **2019**, *5*, 46.
[34] H. Kuang, Z. Xu, X. Tan, K. Yu, C. Chen, *Small* **2024**, *20*, 2308421.
[35] Z. Liu, Y. Du, R. Yu, M. Zheng, R. Hu, J. Wu, Y. Xia, Z. Zhuang, D. Wang, *Angew. Chem.* **2023**, *135*, 202212653.
[36] Y. Liu, L. Li, L. Wang, N. Li, X. Zhao, Y. Chen, T. Sakthivel, Z. Dai, *Nat. Commun.* **2024**, *15*, 2851.
[37] L. Wang, H. Liu, J. Zhuang, D. Wang, *Small Sci.* **2022**, *2*, 2200036.
[38] H. Zhao, D. Zhang, Y. Yuan, X. Wu, S. Li, Z. Li, J. Lai, L. Wang, *Appl. Catal.B: Environ.* **2022**, *304*, 120916.
[39] H. Dong, Y. C. Chen, C. Feldmann, *Green Chem.* **2015**, *17*, 4107.
[40] S. Perumal, I. Pokhrel, U. Muhammad, X. Shao, Y. Han, M. Kim, H. Lee, *ACS Mater. Lett.* **2024**, *6*, 3625.
[41] R. Tachibana, K. Zhang, Z. Zou, S. Burgener, T. R. Ward, *ACS Sustain. Chem. Eng.* **2023**, *11*, 12336.
[42] M. Ghorbani, M. Boley, P. N. H. Nakashima, N. Birbilis, *Sci. Rep.* **2024**, *14*, 8299.
[43] B. Rohr, H. S. Stein, D. Guevarra, Y. Wang, J. A. Haber, M. Aykol, S. K. Suram, J. M. Gregoire, *Chem. Sci.* **2020**, *11*, 2696.
[44] S. Lundberg, Arxiv 1705.07874**2017**.
[45] T. Vinchurkar, J. Ock, A. B. Farimani, arXiv 2405.20397 **2024**.
[46] L. Van der Maaten, G. Hinton, *J. Mach. Learn. Res.* **2008**, *9*, 2605.
[47] S. Anantharaj, S. Noda, M. Driess, P. W. Menezes, *ACS Energy Lett.* **2021**, *6*, 1607.
[48] P. Li, X. Wan, J. Su, W. Liu, Y. Guo, H. Yin, D. Wang, *ACS Catal.* **2022**, *12*, 11667.
[49] D. V. Shinde, L. D. Trizio, Z. Dang, M. Prato, R. Gaspari, L. Manna, *Chem. Mater.* **2017**, *29*, 7032.
[50] J. Baek, M. D. Hossain, P. Mukherjee, J. Lee, K. T. Winther, J. Leem, Y. Jiang, W. C. Chueh, M. Bajdich, X. Zheng, *Nat. Commun.* **2023**, *14*, 5936.
[51] Z. Jin, X. Zhou, Y. Hu, X. Tang, K. Hu, K. M. Reddy, X. Lin, H. J. Qiu, *Chem. Sci.* **2022**, *13*, 12056.
[52] T. Wu, M. Y. Han, Z. J. Xu, *ACS Nano* **2022**, *16*, 8531.
[53] R. Nandan, H. Nara, H. N. Nam, Q. M. Phung, Q. P. Ngo, J. Na, J. Henzie, Y. Yamauchi, *Adv. Sci.* **2024**, *11*, 2402518.
[54] G. Feng, F. Ning, J. Song, H. Shang, K. Zhang, Z. Ding, P. Gao, W. Chu, D. Xia, *J. Am. Chem. Soc.* **2021**, *143*, 17117.
[55] J. Kitagawa, S. Hamamoto, N. Ishizu, *Metals* **2020**, *10*, 1078.
[56] Y. Sharma, B. L. Musico, X. Gao, C. Hua, A. F. May, A. Herklotz, A. Rastogi, D. Mandrus, J. Yan, H. N. Lee, M. F. Chisholm, *Phys. Rev. Mater.* **2018**, *2*, 060404.
[57] P. Sherwood, *Surf. Sci. Spectra.* **1998**, *5*, 1.
[58] E. Paparazzo, *Carbon* **2013**, *63*, 578.
[59] M. Elrouby, M. Abdelsamie, A. El-sayed, *Int. J. Hydrogen Energy* **2023**, *48*, 27960.
[60] J. A. Torres-Ochoa, D. Cabrera-German, O. Cortazar-Martinez, M. Bravo-Sanchez, G. Gomez-Sosa, A. Herrera-Gomez, *Appl. Surf. Sci.* **2023**, *622*, 156960.

© 2025 The Author(s). Advanced Functional Materials published by Wiley-VCH GmbH

16163028, 0, Downloaded from https://advanced.onlinelibrary.wiley.com/doi/10.1002/adfm.202424887 by Junhyeok Seo - Gwangju Institute Of Science And Technology (Gist) , Wiley Online Library on [18/03/2025]. See the Terms and Conditions (https://onlinelibrary.wiley.com/terms-and-conditions) on Wiley Online Library for rules of use; OA articles are governed by the applicable Creative Commons License

[61] Y. Zhang, K. Nie, B. Li, L. Yi, C. Hu, Z. Wang, X. Hao, W. Zhang, Z. Liu, W. Huang, *Appl. Catal. B: Environ. Energy* **2025**, *360*, 124529.
[62] S. Perumal, J. Seo, *Int. J. Hydrogen Energy* **2023**, *48*, 22009.
[63] Y. Yao, Q. Dong, A. Brozena, J. Luo, J. Miao, M. Chi, C. Wang, I. G. Kevrekidis, Z. J. Ren, J. Greeley, G. Wang, *Science* **2022**, *376*, eabn3103.
[64] J. Hu, T. Guo, X. Zhong, J. Li, Y. Mei, C. Zhang, Y. Feng, M. Sun, L. Meng, Z. Wang, B. Huang, *Adv. Mater.* **2024**, *36*, 2310918.
[65] L. Moriau, I. Marić, M. Bele, A. Logar, N. Hodnik, A. K. Surca, *Int. J. Hydrogen Energy* **2025**, *100*, 214.
[66] S. Perumal, T. Lim, S. Seenivasan, J. Seo, *Appl. Surf. Sci.* **2022**, *604*, 154553.
[67] M. Liu, B. A. Lu, G. Yang, P. Yuan, H. Xia, Y. Wang, K. Guo, S. Zhao, J. Liu, Y. Yu, W. Yan, *Adv. Sci.* **2022**, *9*, 2200147.
[68] Y. Huang, X. Mao, G. Yuan, D. Zhang, B. Pan, J. Deng, Y. Shi, N. Han, C. Li, L. Zhang, L. Wang, L. He, Y. Li, Y. Li, *Angew. Chem., Int. Ed.* **2021**, *60*, 15844.
[69] L. Yao, F. Zhang, S. Yang, H. Zhang, Y. Li, C. Yang, H. Yang, Q. Cheng, *Adv. Mater.* **2024**, *36*, 2314049.
[70] F. Pedregosa, G. Varoquaux, A. Gramfort, V. Michel, B. Thirion, O. Grisel, M. Blondel, P. Prettenhofer, R. Weiss, V. Dubourg, J. Vanderplas, A. Passos, D. Cournapeau, M. Brucher, M. Perrot, E. Duchesnay, *J. Mach. Learn. Res.* **2011**, *12*, 2825.

© 2025 The Author(s). Advanced Functional Materials published by Wiley-VCH GmbH

16163028, 0, Downloaded from https://advanced.onlinelibrary.wiley.com/doi/10.1002/adfm.202424887 by Junhyeok Seo - Gwangju Institute Of Science And Technology (Gist) , Wiley Online Library on [18/03/2025]. See the Terms and Conditions (https://onlinelibrary.wiley.com/terms-and-conditions) on Wiley Online Library for rules of use; OA articles are governed by the applicable Creative Commons License